

Background-limited long wavelength infrared InAs/InAs_{1-x}Sb_x type-II superlattice-based photodetectors operating at 110 K

Abbas Haddadi, Arash Dehzangi, Sourav Adhikary, Romain Chevallier, and Manijeh Razeghi^a

Center for Quantum Devices, Department of Electrical Engineering and Computer Science, Northwestern University, Evanston, Illinois 60208, USA

(Received 26 October 2016; accepted 6 January 2017; published online 13 February 2017)

We report the demonstration of high-performance long-wavelength infrared (LWIR) nBn photodetectors based on InAs/InAs_{1-x}Sb_x type-II superlattices. A new saw-tooth superlattice design was used to implement the electron barrier of the photodetectors. The device exhibited a cut-off wavelength of $\sim 10 \mu\text{m}$ at 77 K. The photodetector exhibited a peak responsivity of 2.65 A/W, corresponding to a quantum efficiency of 43%. With an $R \times A$ of 664 $\Omega\text{-cm}^2$ and a dark current density of $8 \times 10^{-5} \text{ A/cm}^2$, under -80 mV bias voltage at 77 K, the photodetector exhibited a specific detectivity of $4.72 \times 10^{11} \text{ cm}\cdot\sqrt{\text{Hz}}/\text{W}$ and a background-limited operating temperature of 110 K. © 2017 Author(s). All article content, except where otherwise noted, is licensed under a Creative Commons Attribution (CC BY) license (<http://creativecommons.org/licenses/by/4.0/>). [<http://dx.doi.org/10.1063/1.4975619>]

Type-II strained-layer superlattices (T2SLs) have become an increasingly active topic of research since their conception by Sai-Halasz *et al.*¹ This material system has demonstrated itself as a viable candidate in many different fields such as lasers, photodetectors,² and phototransistors.³ The type-II band alignment enables full control of the electronic bandstructure by the spatial separation of electrons and holes into different quantum wells; this allows for great flexibility in hetero-structure device design.⁴ InAs/Ga(In)Sb superlattices are, perhaps, the most well-studied member of the T2SLs family. They have become a strong candidate to replace the state-of-the-art mercury-cadmium-telluride (MCT) material system for infrared detection and imaging.^{2,5} However, InAs/InAs_{1-x}Sb_x type-II superlattices have been proven to have longer carrier lifetimes than InAs/GaSb T2SLs⁵⁻⁷ and have been proposed as another alternative for infrared detection. Tremendous effort has been spent on developing sensitive infrared photodetectors based on InAs/InAs_{1-x}Sb_x T2SLs; however, these photodetectors are still facing many challenges, especially in the long-wavelength infrared (LWIR), and therefore, have only shown limited performance in recent reports.⁸⁻¹⁰

LWIR detection is important because the ambient temperature of a scene, for ground-based applications, is around 300 K, where the emission peak is $\sim 9.8 \mu\text{m}$ —at the center of the LWIR atmospheric transmission window; this leads to a demand for sensitive LWIR photodetectors. The challenge for making LWIR photodetectors in this material system is reduction of its dark current density while maintaining good optical quantum efficiency in order to achieve background limited (photon-noise) infrared photodetection (BLIP).

In this work, we present LWIR nBn photodetectors¹¹ based on InAs/InAs_{1-x}Sb_x T2SLs with a new barrier design that has shown a significant dark current reduction compared to prior results⁸ while maintaining low bias-dependent optical response. Thanks to the new barrier design, this nBn photodetector is BLIP at 77 K operating temperature and it stays BLIP up to 110 K.

The proposed nBn device architecture consists of two *n*-doped LWIR superlattices and a thin electron barrier which has zero valence band discontinuity with respect to the *n*-type LWIR regions. One of the *n*-type regions acts as the LWIR absorption region and the other one is used as a contact.

^aAuthor to whom correspondence should be addressed. Electronic mail: razeghi@eecs.northwestern.edu



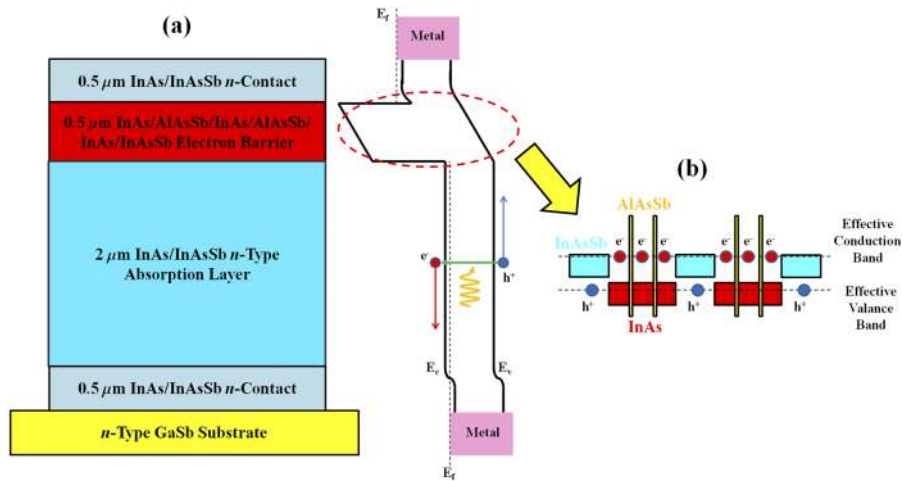


FIG. 1. (a) The schematic diagram and working principle of the nBn photodetector. The barrier blocks the transport of the majority electrons, while allowing the diffusion of minority holes and photo-generated carriers from the absorption region. (b) The band alignment and the creation of an effective bandgap in InAs/AlAs_{1-x}Sb_x/InAs/AlAs_{1-x}Sb_x/InAs/InAs_{1-x}Sb_x saw-tooth superlattice of the barrier. (Colored rectangles represent the forbidden bandgap of the semiconductor materials.) The atomic engineering capabilities of T2SLs enable perfect alignment in the valence bands of the absorption region and the barrier.

Figure 1(a) shows a schematic of the device design and the alignment of the conduction and valence bands. The LWIR superlattice design consists of 30/10 mono-layers (MLs) of InAs/InAs_{0.50}Sb_{0.50}, respectively, per period with a $\sim 10 \mu\text{m}$ nominal cut-off wavelength at 77 K while the electron barrier design consists of 4/3/4/3/4/9 MLs of InAs/AlAs_{0.50}Sb_{0.50}/InAs/AlAs_{0.50}Sb_{0.50}/InAs/InAs_{0.50}Sb_{0.50}, respectively, per period with a nominal cut-off wavelength of $\sim 4 \mu\text{m}$. Using AlAs_{0.50}Sb_{0.50} instead of AlAs in the barrier design⁸ provides more flexibility. Because AlAs_{0.50}Sb_{0.50} has a lower lattice mismatch to the GaSb substrate, it introduces less local strain to the crystalline structure of the superlattice and can be grown thicker compared to AlAs. Furthermore, inserting two spatially separated AlAs_{0.50}Sb_{0.50} high-bandgap layers inside the InAs quantum well (see Figure 1(b)) helps us to achieve a larger effective conduction band offset ($\sim 200 \text{ meV}$) compared to previous work⁸ ($\sim 150 \text{ meV}$) while maintaining high crystalline quality. We call this structure a saw-tooth superlattice.

The device was grown on a Te-doped *n*-type (10^{17} cm^{-3}) GaSb wafer using a solid source molecular beam epitaxy (SSMBE) reactor equipped with group III SUMO[®] cells and group-V valved crackers. The growth started with a 100 nm GaSb buffer layer to smooth out the surface, then, a $0.5 \mu\text{m}$ *n*-doped InAs_{0.91}Sb_{0.09} buffer layer (10^{18} cm^{-3}) was grown, which was followed by a $0.5 \mu\text{m}$ *n*-contact (10^{18} cm^{-3}), a $2 \mu\text{m}$ -thick *n*-type absorption region (10^{16} cm^{-3}), a $0.5 \mu\text{m}$ electron barrier, and a $0.5 \mu\text{m}$ *n*-contact. The *n*-contacts and the absorption region share the same superlattice design and silicon (Si) was used as the *n*-type dopant in this device.

After the epitaxial growth, the material quality was assessed using high resolution X-ray diffraction (HR-XRD) and atomic force microscopy (AFM). The satellite peaks in the HR-XRD scan show that the overall periods of the absorption region and barrier superlattices were about 118 and 79 Å, respectively. The lattice mismatch between the GaSb substrate and the device structure was less than 1000 ppm, as we expected. The AFM showed a good surface morphology with clear atomic steps and a root mean squared (RMS) roughness of 1.2 Å over a $10 \times 10 \mu\text{m}^2$ area.

After material quality assessment, the grown material was processed into a set of unpassivated mesa-isolated test structures with device sizes ranging from 100×100 to $400 \times 400 \mu\text{m}^2$ using standard photo-lithographic processing technique followed by mesa definition using BCl₃:Ar⁺ dry etching and citric acid treatment to remove dry etch residues. Top and bottom metal contacts were formed using electron beam deposited Ti/Pt/Au. The photodetectors were left unpassivated but special attention was paid during the processing steps by performing many surface cleaning steps using different solvents in order to minimize the surface leakage. Then, the sample was wire-bonded to a

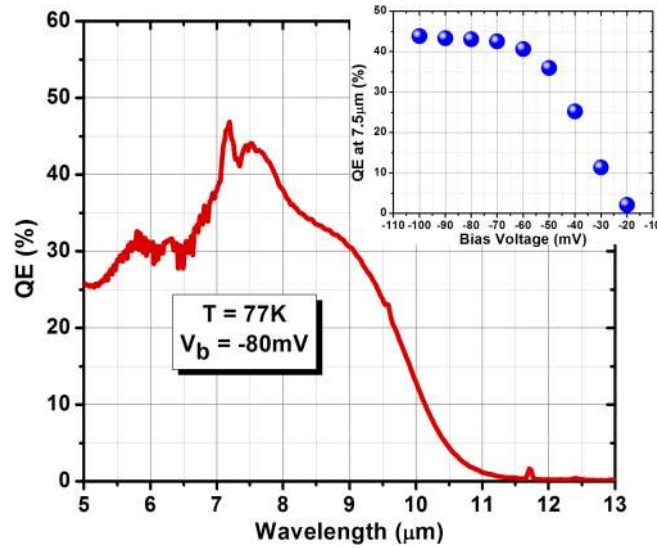


FIG. 2. Saturated quantum efficiency spectrum of the device at -80 mV applied bias voltage in front-side illumination configuration without any anti-reflection coating. Inset: Quantum efficiency of the device at 7.5 μm in front-side illumination configuration as a function of applied bias voltage (V_b).

68 pin leadless ceramic chip carrier (LCCC) and loaded into a cryostat for both optical and electrical characterization at temperatures ranging from 77 to 130 K.

The optical characterization was done at temperatures between 77 and 130 K under front-side illumination without any anti-reflection (AR) coating having been applied to the photodetector. A Bruker IFS 66 v/S Fourier transform infrared spectrometer (FTIR) was used to measure the spectral response of the photodetectors. The responsivity and quantum efficiency of the photodetector were measured using a calibrated blackbody source at 1000 $^{\circ}\text{C}$. Figure 2 shows the optical performance; the device exhibits a 50% cut-off wavelength of ~ 10 μm at 77 K (see Figure 2 inset) which corresponds with the designed band structure. The device responsivity reaches a peak of 2.65 A/W, corresponding to quantum efficiency (QE) of 43% for a device with 2 μm -thick absorption region. An applied bias voltage is required in this device to extract the full optical signal which is a characteristic of an nBn unipolar device. This bias voltage is usually high ($V_b > 500$ mV) for nBn devices⁹ because of the large valence band discontinuity between the absorption layer and the electron barrier; but, this device requires much lower bias voltage to fully extract the optical signal because the new saw-tooth superlattice-based barrier leads to nearly perfect valence band continuity. The QE starts to increase linearly with increasing reverse bias voltage from 20 mV and saturates at 80 mV, as shown in the inset of Figure 2. This is a very good saturation value for an nBn device, and will allow the devices to be operated at small dark currents.

Figure 3 shows the electrical performance of the nBn device measured when covered by a cold-shield. Figure 3(a) presents the dark current density versus applied bias voltage characteristics of the device at different temperatures ranging from 77 to 130 K. At 77 K, the sample exhibits a dark current density of 8×10^{-5} A/cm² under -80 mV applied bias and a differential-resistance area product ($R \times A$) of 664 $\Omega\text{-cm}^2$ under the same bias voltage. The variation of $R \times A$ versus inverse temperature ($1/T$) from 77 to 130 K is shown in Figure 3(b). Below 100 K, the $R \times A$ exhibits an Arrhenius-type behavior with extracted associated activation energy of about ~ 75 meV which is smaller than the bandgap energy of the photodetector (~ 124 meV). This indicates that the dark current of the device is not completely dominated by the diffusion mechanism below 100 K. However, above 100 K the device electrical performance becomes totally diffusion-limited. This behavior suggests that there is still room for further improvement in the electrical performance of the photodetectors at temperatures below 100 K by suppressing dark current mechanisms such as generation-recombination (G-R).¹²

After the electrical and optical characterization, the specific detectivity was calculated by taking into account both the Johnson thermal noise and the electrical shot noise at the operational bias.

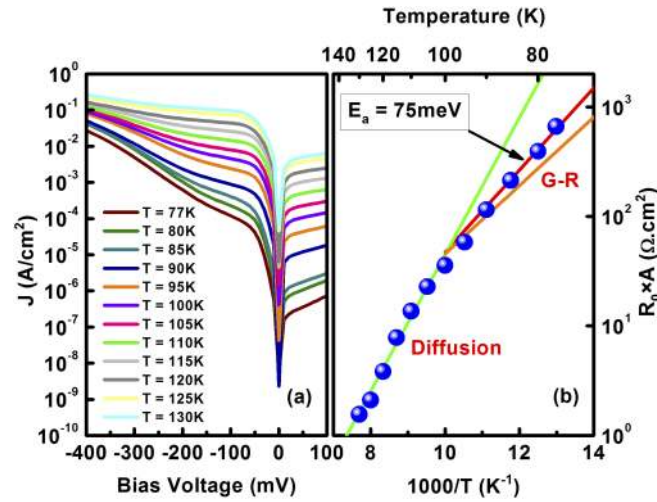


FIG. 3. (a) Dark current density vs. applied bias voltage characteristic of the sample as a function of temperature. (b) $R \times A$ vs. $1/T$; the sample exhibited an Arrhenius type behavior with an associated activation energy (E_a) of about ~ 75 meV below 100 K. At temperatures above 100 K, the device dark current is completely diffusion-limited. The green and orange lines represent the expected diffusion and generation-recombination (G-R) limits, respectively.

The devices exhibit saturated dark current shot noise limited specific detectivity (D^*) of 4.72×10^{11} cm $\cdot\sqrt{\text{Hz}}/\text{W}$ (at a peak responsivity of $7.5 \mu\text{m}$) under -80 mV of applied bias (Figure 4). In order to determine the BLIP temperature, we used the point when the specific detectivity of the photodetector is less than the value for an ideal photodetector with 100% QE and a fully immersed 300 K background with a 2π field of view (FOV).¹³ Figure 4 (inset) presents the specific detectivity of the photodetector at $7.5 \mu\text{m}$ versus operating temperature. As the temperature increases, the specific detectivity reduces and intersects the BLIP specific detectivity (green line) slightly beyond 110 K.

In conclusion, we have reported the design, growth, and characterization of high-performance LWIR nBn photodetectors based on InAs/InAs_{1-x}Sb_x T2SLs on GaSb substrates. A new saw-tooth

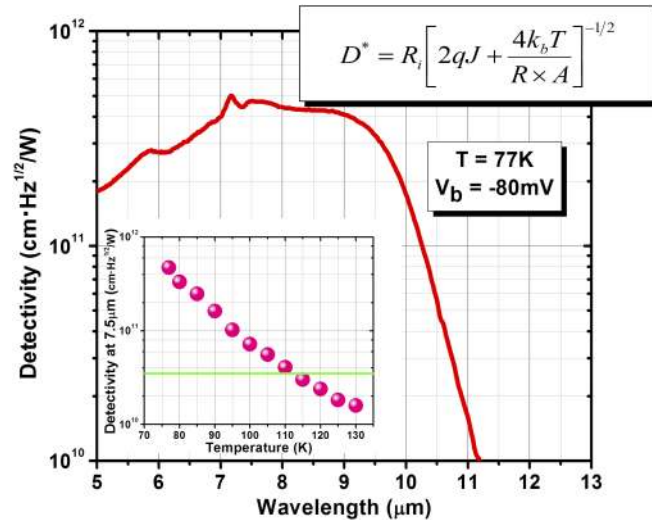


FIG. 4. Saturated specific detectivity spectrum of the device at -80 mV applied bias voltage in front-side illumination configuration without any anti-reflection coating. Inset: Specific detectivity of the device versus operating temperature at $7.5 \mu\text{m}$ under front-side illumination. The green line is the BLIP detectivity for an ideal photodetector with 2π FOV with 300 K background. The specific detectivity is calculated based on the equation in the inset, where R_i is the device responsivity, J is the dark current density, $R \times A$ is the differential resistance \times area product, k_b is the Boltzmann constant, and T is the operating temperature.

superlattice design was used to implement the electron barrier of the device. The devices exhibited a 50% cut-off wavelength of $10\ \mu\text{m}$ at 77 K. At the peak responsivity, the photodetector exhibited QE and responsivity of 43% and $2.65\ \text{A/W}$, respectively, under front-side illumination and without any AR coating. At $-80\ \text{mV}$, the device exhibited dark current density and $R \times A$ of $8 \times 10^{-5}\ \text{A/cm}^2$ and $664\ \Omega\text{-cm}^2$, respectively, at 77 K. At $7.5\ \mu\text{m}$, the device exhibited a saturated dark current shot noise limited specific detectivity of $4.72 \times 10^{11}\ \text{cm}\cdot\sqrt{\text{Hz}}/\text{W}$ at 77 K. Finally, the device showed BLIP performance up to an operating temperature of 110 K; this requires less stringent cooling requirements, which makes T2SL a viable option for third generation FPAs.

¹ G. A. Sai-Halasz, R. Tsu, and L. Esaki, *Appl. Phys. Lett.* **30**, 651 (1977).

² M. Razeghi, U.S. Patent 6864552 (8 March 2005).

³ A. Haddadi, S. Adhikary, A. Dehhangi, and M. Razeghi, *Appl. Phys. Lett.* **109**, 021107 (2016).

⁴ B. M. Nguyen, M. Razeghi, V. Nathan, and G. J. Brown, in *Type-II M Structure Photodiodes: An Alternative Material Design for Mid-Wave to Long Wavelength Infrared Regimes* (SPIE, San Jose, CA, USA, 2007), p. 64790S.

⁵ D. Donetsky, S. P. Svensson, L. E. Vorobjev, and G. Belenky, *Appl. Phys. Lett.* **95**, 212104 (2009).

⁶ B. V. Olson, E. A. Shaner, J. K. Kim, J. F. Klem, S. D. Hawkins, L. M. Murray, J. P. Prineas, M. E. Flatté, and T. F. Boggess, *Appl. Phys. Lett.* **101**, 092109 (2012).

⁷ E. H. Steenberg, B. C. Connelly, G. D. Metcalfe, H. Shen, M. Wraback, D. Lubyshev, Y. Qiu, J. M. Fastenau, A. W. K. Liu, S. Elhamri, O. O. Cellek, and Y.-H. Zhang, *Appl. Phys. Lett.* **99**, 251110 (2011).

⁸ A. Haddadi, G. Chen, R. Chevallier, A. M. Hoang, and M. Razeghi, *Appl. Phys. Lett.* **105**, 121104 (2014).

⁹ H. S. Kim, O. O. Cellek, Z.-Y. Lin, Z.-Y. He, X.-H. Zhao, S. Liu, H. Li, and Y.-H. Zhang, *Appl. Phys. Lett.* **101**, 161114 (2012).

¹⁰ A. Haddadi, R. Chevallier, G. Chen, A. M. Hoang, and M. Razeghi, *Appl. Phys. Lett.* **106**, 011104 (2015).

¹¹ S. Maimon and G. W. Wicks, *Appl. Phys. Lett.* **89**, 151109 (2006).

¹² G. G. Zegrya and A. D. Andreev, *Appl. Phys. Lett.* **67**, 2681 (1995).

¹³ D. Hoffman, B.-M. Nguyen, E. K.-w. Huang, P.-Y. Delaunay, M. Razeghi, M. Z. Tidrow, and J. Pellegrino, *Appl. Phys. Lett.* **93**, 031107 (2008).